Oblique electron fire hose instability: Particle-in-cell simulations

Petr Hellinger,[1] Pavel M. Trávníček,[2,1] Victor K. Decyk,[3] and David Schriver[4,3]

Abstract. Nonlinear properties of the oblique resonant electron fire hose instability are investigated using two-dimensional particle-in-cell simulations in the Darwin approximation for weak initial growth rates. The weak electron fire hose instability has a self-destructive nonlinear behavior; it destabilizes a non-propagating branch which only exists for a sufficiently strong temperature anisotropy. The nonlinear evolution leads to generation of non-propagating waves which in turn scatter electrons and reduce their temperature anisotropy. As the temperature anisotropy is being reduced, the non-propagating branch disappears and the generated standing waves are transformed to propagating whistler waves which are rapidly damped. Consequently, the oblique electron fire hose efficiently reduces the electron temperature anisotropy.

1. Introduction

Solar wind electrons exhibit important nonthermal features including multiple populations drifting with respect to each other and temperature anisotropies, even though they are relatively strongly coupled through Coulomb collisions [*Phillips et al.*, 1989; *Phillips and Gosling*, 1990; *Salem et al.*, 2003]. The temperature anisotropies are a source of free energy for many different instabilities [*Gary*, 1993]. For the temperature anisotropy $T_{\parallel e} > T_{\perp e}$ (for symbol definitions see Appendix) the dominant instability (for moderately magnetized plasmas) is the oblique resonant non-propagating electron fire hose [*Li and Habbal*, 2000; *Gary and Nishimura*, 2003]. Competing nonresonant/propagating fire hose modes [*Hollweg and Völk*, 1970; *Paesold and Benz*, 1999, 2003] have typically lower growth rates and higher thresholds close to the fluid one [*Gary and Nishimura*, 2003]. Other competing instabilities such as the Weibel instability [*Lazar and Poedts*, 2009; *Ibscher et al.*, 2012; *Lazar et al.*, 2013] may reach much larger growth rates, but typically have a much higher threshold than the oblique fire hose instability (except in very high beta/unmagnetized plasmas). The oblique electron fire hose destabilizes non-propagating oblique modes which appear as a result of branch change from the propagating whistler waves. The most unstable mode appears at oblique angles (with respect to the ambient magnetic field) and at electron inertial scales; the angle of propagation decreases and wavelength increases when approaching the threshold [*Camporeale and Burgess*, 2008]. This instability is resonant with electrons (through both the standard and anomalous cyclotron resonances) and is unstable even for $\beta_{\parallel e} - \beta_{\perp e} < 2$, i.e., below the fluid fire hose threshold.

In situ observations indicate a presence of bounds on the temperature anisotropy of the electron core and halo populations. These bounds are compatible with linear predictions for the dominant oblique resonant fire hose calculated for a single electron bi-Maxwellian velocity distribution function [*Štverák et al.*, 2008]. In order to understand the role of this instability in the solar wind, its nonlinear properties need to be considered. The nonlinear properties of the oblique electron fire hose instability are not well understood. Only a small number of simulations of electron fire hose instabilities have been performed to date. *Messmer* [2002] and *Paesold and Benz* [2003] investigated the nonresonant fire hose instability, but only for parallel propagation.

Gary and Nishimura [2003] studied the oblique resonant fire hose instability in strongly unstable cases (with initial conditions well above the fluid threshold which leads to large growth rates $\sim 0.2\omega_{ce}$) using one-dimensional (1-D) explicit particle-in-cell (PIC) simulations with a relatively small box (with a size four times the wavelength of the fastest growing mode). *Gary and Nishimura* [2003] terminated their simulations shortly after the saturation, i.e., shortly after fluctuating magnetic energy reached the maximum. At that time the states of the 1-D simulations were near the theoretical marginal stability. *Gary and Nishimura* [2003] reported only the presence of non-propagating modes in their simulations.

Camporeale and Burgess [2008] used 1-D and two-dimensional (2-D) implicit PIC simulations of strong fire hose instabilities ($\gamma \gtrsim 0.25\omega_{ce}$) using small simulation boxes (chosen so that two and four wavelengths of the fastest growing mode fit into the box in 2-D and 1-D cases, respectively). *Camporeale and Burgess* [2008] observed a complex evolution of the simulated system. The generated wave activity shifts during the nonlinear evolution to smaller propagation angles and larger wavelengths in agreement with the linear prediction. This property indicates that at least a 2-D simulation for electron fire hose instability is needed. The generated waves become eventually damped and the system exhibits oscillations around marginal stability. Beside the non-propagating modes, *Camporeale and Burgess* [2008] also observed the generation of propagating modes which they attribute to the competing propagating branch as they are also linearly destabilized. Such a behavior was not observed by *Gary and Nishimura* [2003] likely due to the limitations of the 1-D geometry and the short duration.

These previous simulations were limited by small simulation box sizes; since only a few unstable modes were allowed within the simulation box size, this may have an important effect on the nonlinear evolution and quasi-linear effects are also likely to be reduced. Also, the use of strong initial growth rates are not very relevant in the solar wind where the electron temperature anisotropy is only slowly driven [cf. *Phillips and Gosling*, 1990]. Furthermore, starting in a region where both non-propagating and propagating modes are unstable complicates the analysis and interpretation of the simulation results. To overcome the limitations of the previous simulation results we investigate in this paper nonlinear properties of the resonant non-propagating oblique electron fire hose using explicit 2-D PIC code in the Darwin approximation for relatively weak growth rates and a large simulation box with respect to the fastest growing mode. This paper is organized as follows: section 2 briefly summarizes linear theory predictions, section 3 describes the numerical code and simulation results. In section 4 we discuss the presented results.

[1] Astronomical Institute and Institute of Atmospheric Physics, AS CR, Prague, Czech Republic.

[2] Space Sciences Laboratory, University of California, Berkeley, USA.

[3] Department of Physics and Astronomy, University of California, Los Angeles, California, USA.

[4] Institute of Geophysics and Planetary Physics, University of California, Los Angeles, California, USA.

2. Linear theory

The linear dispersion of the whistler mode becomes complicated when electrons exhibit a temperature anisotropy $T_{e\parallel} > T_{e\perp}$. For a large enough temperature anisotropy, non-propagating modes appear due to a branch change from the propagating whistler mode. The non-propagating modes may become unstable for a sufficiently strong electron temperature anisotropy [*Li and Habbal*, 2000]; This instability is called here oblique (resonant) electron fire hose. For stronger temperature anisotropies propagating modes also become unstable [*Li and Habbal*, 2000; *Camporeale and Burgess*, 2008]. An example of the whistler/fire hose dispersion behavior for weak growth rates is shown in Figure 1. Figure 1 displays a dispersion relation $\omega_r = \omega_r(k)$ (solid line) and $\gamma = \gamma(k)$ (dashed line) for the parallel propagation $\theta_{kB} = 0°$ (left panel) and $\theta_{kB} = 64°$ (right panel); the plasma is assumed to consist of anisotropic electrons and isotropic protons with the following parameters: the parallel electron beta $\beta_{\parallel e} = 2$, the temperature anisotropy $T_{\perp e}/T_{\parallel e} = 0.216$; the frequency ratio is $\omega_{pe}/\omega_{ce} = 4$, and the proton temperature is $T_p = T_{\parallel e}$. In the case of parallel propagation the real frequency ω_r is not a monotonic function of the wave vector k. There exists a local maximum and the ω_r crosses zero and becomes negative. For oblique propagation the real frequency ω_r, becomes zero for a wide range of wave vectors, and a part of this branch is unstable (in this case the propagating modes are stable). The branch change from the propagating whistler waves to non-propagating modes also alters the polarization; while the propagating whistler waves have a circular/elliptical polarization the non-propagating branch has a linear Alfvénic polarization (i.e., the fluctuating magnetic field is perpendicular with respect to both the ambient magnetic field and the wave vector).
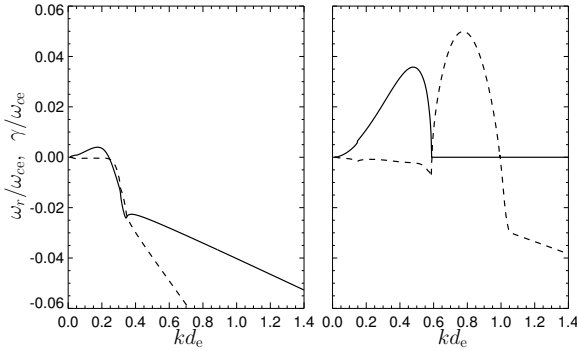

Figure 1. Dispersion relation of the whistler mode: The real frequency $\omega_r = \omega_r(k)$ (solid line) and the growth rate $\gamma = \gamma(k)$ (dashed line) for the parallel propagation $\theta_{kB} = 0°$ (left panel) and for $\theta_{kB} = 64°$ (right panel).

These dispersive properties of the electron oblique resonant fire hose instability are similar to those of the proton oblique resonant fire hose instability [cf., *Hellinger and Matsumoto*, 2000]. Therefore, we expect that the two instabilities have a similar nonlinear evolution.

3. Numerical simulations

3.1. Simulation model and parameters

To investigate nonlinear properties of the electron fire hose instability we use a 2-D version of an explicit electromagnetic PIC code that employs the Darwin approximation [*Decyk*, 2007],schral10. The Darwin PIC model neglects the transverse component of the displacement current (but keeps the longitudinal part) in the full set of Maxwell's equations, which makes them radiation-free, but leaves the whistler physics unaffected from its fully electromagnetic counterpart [*Hewett*, 1985]; namely, the electric field is separated into transverse and longitudinal components

$$E = E_T + E_L \qquad (1)$$

where $\nabla \times E_L = 0$ and $\nabla \cdot E_T = 0$ and the Maxwell equations are modified as

$$\nabla \cdot E_L = \frac{\rho}{\epsilon_0}, \quad \nabla \times E_T = -\frac{\partial B}{\partial t} \qquad (2)$$

$$\nabla \cdot B = 0, \quad \nabla \times B = \frac{1}{c^2}\frac{\partial E_L}{\partial t} + \mu_0 j. \qquad (3)$$

The radiation-free Darwin approximation removes the demanding Courant-Friedrich-Levy condition for a time step given by the speed of light (and the size of the grid used) [*Schriver et al.*, 2010]. Consequently, the time step is set by the greater of the electron plasma frequency or the electron cyclotron frequency.

Here we use the real mass ratio $m_p/m_e = 1836$ and for the frequency ratio we use $\omega_{pe}/\omega_{ce} = 4$. The electrons have initially $\beta_{\parallel e} = 2$ and $T_{\perp e}/T_{\parallel e} = 0.216$ whereas the protons are initially isotropic with $T_p = T_{\parallel e}$. The simulation box is chosen to be a 2-D grid 2048×1024 with the physical sizes $512 d_e \times 256 d_e$. The magnetic field is chosen to be along the x-direction. The parallel (x) and perpendicular (y) simulation box sizes are about 28 times the scales $2\pi/k_{\parallel max}$ and $2\pi/k_{\perp max}$ of the fastest growing mode, respectively. There are 1024 macroparticles per cell for electrons and 512 macroparticles per cell for protons. The time step is $\Delta t = 0.025\omega_{ce}^{-1}$.

3.2. Simulation results

The initial condition $\beta_{\parallel e} = 2$ and $T_{\perp e}/T_{\parallel e} = 0.216$ are unstable with respect to the oblique fire hose instability (see Figure 3) with the maximum growth rate $\gamma_{max} = 0.05\omega_{ce}$ which appears at $k_{max} = 0.778/d_e$ and $\theta_{kB max} = 64.1°$. The unstable electron distribution function generates non-propagating waves which in turn scatter electrons. The time evolution of the electron macroscopic properties are show in Figure 2.

Figure 2 shows in the top and middle panels the electron temperature anisotropy $T_{\perp e}/T_{\parallel e}$ and the electron parallel beta $\beta_{\parallel e}$ as functions of time. The temperature anisotropy decreases with time ($T_{\perp e}/T_{\parallel e}$ increases) and the $\beta_{\parallel e}$ decreases. A part of the parallel electron kinetic energy is transferred to the perpendicular kinetic energy and to the wave energy. In the bottom panel of Figure 2 the solid line shows the evolution of the maximum growth rate of the fire hose instability calculated from the evolving velocity distribution function; the electron velocity distribution function is calculated on a 2-D velocity grid 512×512 for $-5v_{th\parallel e} \leq v_\parallel \leq v_{th\parallel e}$ and $0 \leq v_\perp \leq v_{th\parallel e}$ and is used for the calculation of the dispersion relation $\det D = 0$ where

$$D = \left(1 - \frac{k^2 c^2}{\omega^2} - \sum_{s\in\{p,e\}} \frac{\omega_{ps}^2}{\omega^2}\right) \mathbf{1} + \frac{kk c^2}{\omega^2} \qquad (4)$$

$$- \sum_{s\in\{p,e\}} \frac{\omega_{ps}^2}{\omega^2} \sum_{n=-\infty}^{\infty} \int \frac{k_\parallel \frac{\partial f_s}{\partial v_\parallel} + n\frac{\omega_{cs}}{v_\perp}\frac{\partial f_s}{\partial v_\perp}}{k_\parallel v_\parallel - \omega + n\omega_{cs}} \overline{w_{sn}} w_{sn} d^3 v$$

and

$$w_{sn} = \left(nJ_n \frac{\omega_{cs}}{k_\perp}, iJ_n' v_\perp, J_n v_\parallel\right). \qquad (5)$$

Protons are assumed to be Maxwellian and the discrete electron velocity distribution is used; the integration over the electron velocity distribution is replaced by a summation over the velocity grid, and the summation over resonances for electrons goes from $n = -20$ to $n = 20$ [cf., *Hellinger and Trávníček*, 2011, for more details]. For comparison the dashed line denotes the maximum growth rate calculated from the temperatures assuming that the electron velocity distribution remains bi-Maxwellian. The maximum growth rate (calculated from the velocity distribution function) first remains close to the initial value $0.05\omega_{ce}$, then it somewhat surprisingly temporarily increases and reaches the maximum value $0.069\omega_{ce}$ at $t = 114/\omega_{ce}$ and after that the maximum growth

rate decreases. The transient increase of the maximum growth rate may be a problem of the discrete approximation; however, the electron velocity distribution function varies only weakly on scales much larger than the grid resolution and the initial results from the discrete solver are in a good agreement the linear prediction for the electron bi-Maxwellian velocity distribution function. The system becomes linearly stabilized at around $t = 220/\omega_{ce}$. The bi-Maxwellian maximum growth rate initially follows closely the maximum growth rate obtained from the distribution function but later decreases faster and reaches zero around $170/\omega_{ce}$.

The sharp decrease of the maximum growth rate calculated from the velocity distribution function at around $t = 220/\omega_{ce}$ likely indicates a problem with the calculation of the dispersion relation based on the discrete distribution function, but it may be just a signature of some fast transition in the system.
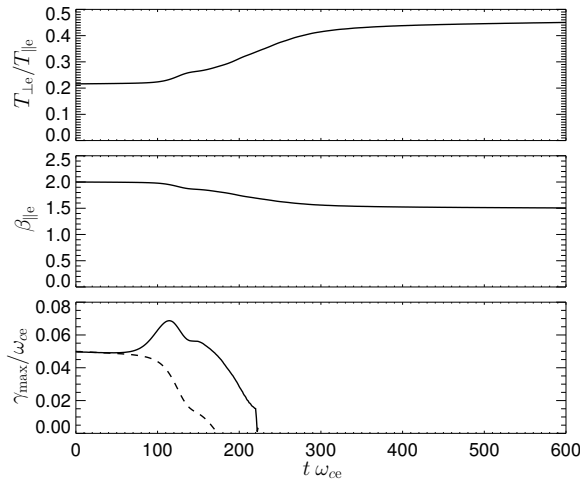

Figure 2. Time evolution of the simulated system: (top) the electron temperature anisotropy, (middle) the electron parallel beta as a function of time and (bottom) the maximum growth rate of the fire hose instability calculated from the electron velocity distribution function (solid) and calculated from the moments assuming a bi-Maxwellian shape (dashed).

The linear predictions at the beginning of the simulation and at the time when the maximum growth rate is the largest (as shown in Figure 2, solid line) are displayed in Figure 3. Figure 3 shows a gray scale plot of the growth rate as a function of the wave vector k and the angle of propagation θ_{kB}, $t = 0$ (left panel) and $t = 114/\omega_{ce}$ (right panel). The results on the left panel were calculated for bi-Maxwellian electrons whereas on the right panel the results were calculated from the actual velocity distribution function. The unstable regions in both the cases follows roughly constant $k_\parallel$ and the unstable modes are non-propagating. The maximum growth rate at $t = 0$ appears at $k_{max} = 0.778/d_e$ and $\theta_{kBmax} = 64.1°$ and reaches the value of $0.05\omega_{ce}$, whereas at $t = 114/\omega_{ce}$ the maximum growth rate is $0.069\omega_{ce}$ for $k_{max} = 0.843/d_e$ and $\theta_{kBmax} = 61.9°$ At $t = 114/\omega_{ce}$ the maximum growth rate is

larger than at the beginning, but the unstable region is narrower in wavenumber and propagation angle range.
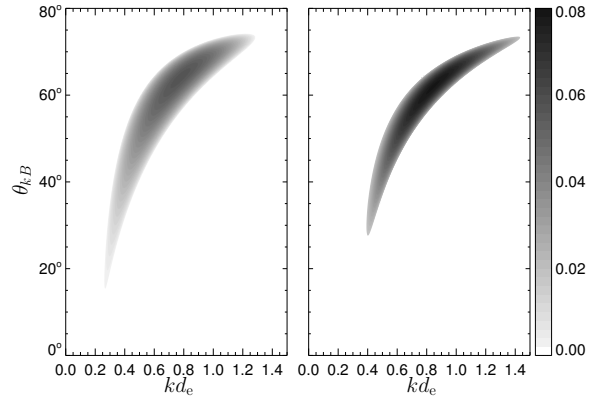

Figure 3. Gray scale plots of the growth rate as a function of the wave vector k and the angle of propagation θ_{kB} at $t = 0$ (left panel) and $t = 114/\omega_{ce}$ (right panel). The growth rate gray scale is shown at the right.

The time evolution of the wave energy is shown in Figure 4. Figure 4 shows in the top panel the fluctuating magnetic field $\delta B^2/B_0^2$ (solid line) as a function of time; (for comparison the energy in the Alvénic component of the fluctuating magnetic field $\delta B_z^2/B_0^2$ is overplotted by the dashed line). The middle and bottom panels display gray scale plots of the fluctuating magnetic field δB as a function of time and wave vector k and as a function of time and propagation angle θ_{kB}, respectively. The solid lines on the middle and bottom panels show the linear prediction, the position of the most unstable mode calculated from the evolving (discrete) electron velocity distribution function (see Figure 2); the dashed lines denote the linear prediction based on the bi-Maxwellian velocity distribution function.

Figure 4 shows that the electron fire hose generates essentially Alvénic fluctuations in agreement with the linear prediction. The unstable modes appear at short wavelengths $k \sim 0.7/d_e$ and strongly oblique propagation angles $\theta_{kB} \sim 60°$. During the evolution the fluctuating fields shift towards less oblique angles in agreement with the linear prediction which shows that the most unstable mode moves to less oblique angles (whereas the wave vectors remain at about the same magnitude or slightly decrease); the bi-Maxwellian results predict smaller wave vectors and a stabilization appears well before the saturation/maximum of $\delta B^2/B_0^2$. The shift of the fluctuating magnetic energy to less oblique angles is to a large extent due to quasi-linear effects as expected from the linear prediction [*Camporeale and Burgess*, 2008]. The rapid change of the wave vector and the propagation angle of the most unstable mode at $t \sim 220/\omega_{ce}$ (related to the fast stabilization) likely indicates problems with the discrete linear dispersion or may be related to a fast change of the dispersion relation.

The fluctuating magnetic field $\delta B^2/B_0^2$ initally grows exponentially as $\propto \exp(0.098t\omega_{ce})$, i.e., slightly slower than what is expected for the most unstable mode (as other, slower growing modes contribute to it). The fluctuating $\delta B^2/B_0^2$ reaches its maximum at around $200/\omega_{ce}$ shortly before the fire hose instability is stabilized (as predicted by the linear analysis based on the evolving electron velocity distribution function, see Figure 2, solid line). During the later evolution most of the initially generated fluctuating wave energy is damped and contributes to perpendicular electron heating (see Figure 2). Some waves appear at parallel propagation probably due to wave-wave interactions.
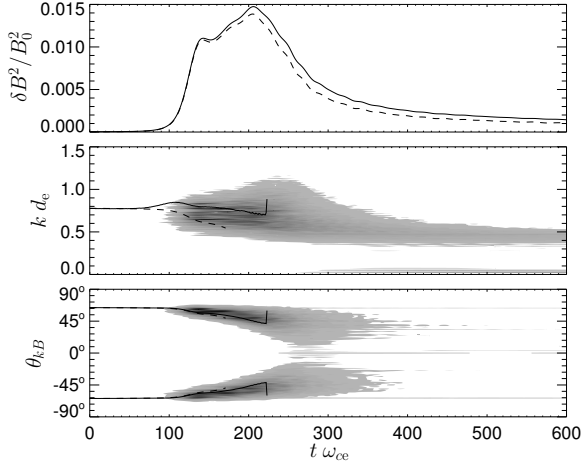
Figure 4. Evolution of the wave spectra: (top) Fluctuating magnetic field $\delta B^2/B_0^2$ (solid line) as a function of time; for comparison $\delta B_z^2/B_0^2$ is overplotted (dashed line). Gray scale plots of the fluctuating magnetic field δB as a function of time and wave vector k (middle panel) and as a function of time and propagation angle θ_{kB} (bottom panel). The solid lines on the middle and bottom panels show the linear prediction, the position of the most unstable mode calculated from the evolving velocity distribution function, whereas the dashed lines show the linear prediction assuming the electron velocity distribution function remains bi-Maxwellian (see Figure 2).

The properties of the fluctuating magnetic field are shown in Figure 5. Figure 5 displays a gray scale plot of the absolute value of the dominant Alfvénic component $|B_z|$ as a function of time and distance l (which was taken through a part of the simulation box along a cut at 45° with respect to the ambient magnetic field). Figure 5 clearly shows that initially the oblique fire hose instability generates standing modes predicted by the linear theory. The non-propagating waves gradually transform themselves to propagating ones and are damped. This may be expected as the non-propagating modes exist only for sufficiently strong temperature anisotropy which is being reduced by the instability (this is an evolution similar to that observed in the case of the oblique proton fire hose instability [*Hellinger and Matsumoto*, 2000]).
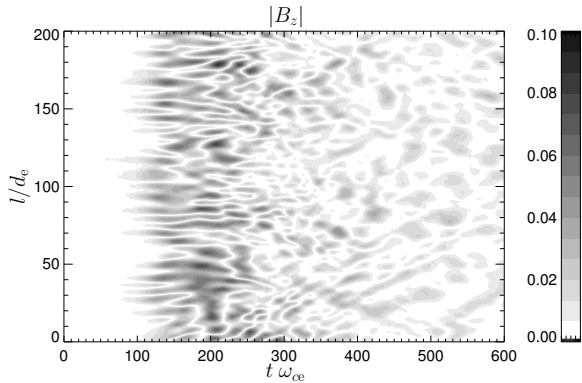

Figure 5. Gray scale plot of the (absolute value of the) dominant component of the magnetic field $|B_z|$ as a function of time and distance l (along a cut through a part of the simulation box at 45° with respect to the ambient magnetic field).

On the macroscopic level the wave-particle interactions due to the instability lead to an effective temperature isotropization. This

isotropization may be characterized by a frequency ν_T given by

$$\frac{\mathrm{d}(T_{\|\mathrm{e}} - T_{\perp\mathrm{e}})}{\mathrm{d}t} = -\nu_T(T_{\|\mathrm{e}} - T_{\perp\mathrm{e}}). \qquad (6)$$

Figure 6 displays on the top panel this isotropization frequency ν_T as a function of time; ν_T reaches a maximum value of about $\nu_T \sim 0.004\omega_{\mathrm{ce}}$ and is roughly proportional to $\delta B^2/B_0^2$ as

$$\nu_T \sim 0.24\frac{\delta B^2}{B_0^2}\omega_{\mathrm{ce}} \qquad (7)$$

(see Figure 4).

Protons are only weakly affected by the electron fire hose instability. Figure 6 (middle and bottom panel) shows the relative changes of the parallel and perpendicular proton temperatures and functions of time. Protons are only slightly heated during the decay phase $t \gtrsim 150/\omega_{\mathrm{ce}}$, the relative increase of $T_{\|\mathrm{p}}$ is about $2.5 \cdot 10^{-4}$ whereas the relative increase of $T_{\perp\mathrm{p}}$ is about $2.0 \cdot 10^{-4}$. This weak proton heating is not surprising. The wave activity appears on short spatial and temporal scales, and, while the non-propagating modes resonate with protons with $v_{\|} \sim 0$ trough the cyclotron resonances, these resonances shift to velocities much larger than the proton thermal velocity for the propagating modes.
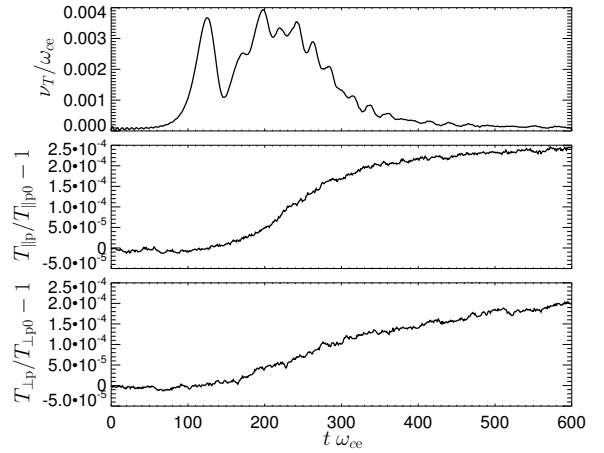

Figure 6. Evolution of the simulated system: (top) the isotropization frequency ν_T as a function of time. The middle and bottom panels show the relative changes of the proton parallel and perpendicular temperatures as functions of time.

On the microscopic level the generated waves interact with mainly (cyclotron) resonant electrons and scatter them in the perpendicular direction. Figure 7 shows gray scale plots of the electron velocity distribution functions at (left) $t = 200\omega_{\mathrm{ce}}^{-1}$ and (right) $t = 600\omega_{\mathrm{ce}}^{-1}$. There are clear signatures of the perpendicular scattering for the resonant electrons with $v_{\|} \sim v_{th\|\mathrm{e}}$.
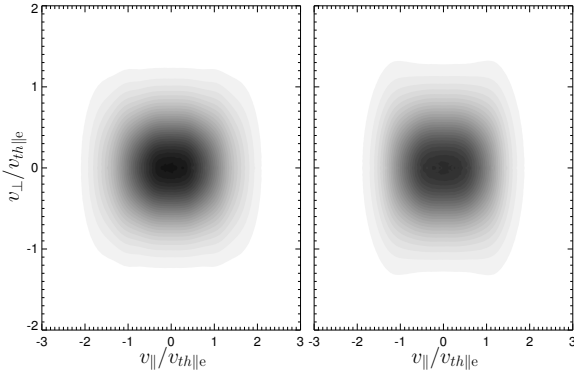
Figure 7. Gray scale plots of the electron velocity distribution functions at (left) $t = 200\omega_{ce}^{-1}$ and (right) $t = 600\omega_{ce}^{-1}$.

The self-destructing behavior leads to an efficient isotropization of electrons and the final stage of the instability is stable with respect to the instability. The system does not end up at the marginal stability. This property is clearly demonstrated in Figure 8 which show paths in ($\beta_{\|e}$, $T_{\perp e}/T_{\|e}$) by the solid lines for the present simulation with the starting point ($\beta_{\|e} = 2$, $T_{\perp e}/T_{\|e} = 0.216$) compared to two other simulations with similar parameters starting at ($\beta_{\|e} = 4$, $T_{\perp e}/T_{\|e} = 0.536$) and ($\beta_{\|e} = 8$, $T_{\perp e}/T_{\|e} = 0.722$). The full and empty circles show the initial and final stages, respectively, and the dotted lines denote the corresponding constant electron energy/temperature contours. The dashed labeled lines denote contours of the constant maximum growth rates (given in units of ω_{ce}). The dash-dotted line denotes the fluid fire hose threshold condition $\beta_{\|e} - \beta_{\perp e} = 2$. Figure 8 clear shows that the oblique electron instability has a threshold lower than the fluid prediction. The marginal stability condition $\gamma_{max} = 10^{-3}\omega_{ce}$ can be approximated (for $1.4 < \beta_{\|e} < 10$) by the relation

$$T_{\perp e}/T_{\|e} = 1 - \frac{1.27}{\beta_{\|e}^{0.954}} \quad (8)$$

[cf., *Gary and Nishimura*, 2003]. The three simulations have an overall similar evolution leading to relatively large jumps in the ($\beta_{\|e}$, $T_{\perp e}/T_{\|e}$) space from the unstable to the stable regions roughly following the constant electron temperature contours; during the evolution electrons lose some of their kinetic energy which they regain at later stages, having about the same kinetic energy at the beginning and at the end of the simulations. The simulation with the initial conditions ($\beta_{\|e} = 8$, $T_{\perp e}/T_{\|e} = 0.722$) starts

slightly above the fluid fire hose threshold, but we do not observe any significant propagating wave activity during the initial phase.
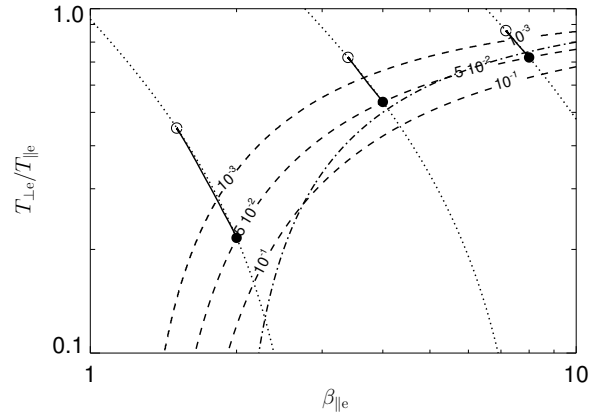

Figure 8. The solid lines denote paths in the ($\beta_{\|e}$, $T_{\perp e}/T_{\|e}$) plane for three simulations starting at $\beta_{\|e} = 2$, $T_{\perp e}/T_{\|e} = 0.216$, $\beta_{\|e} = 4$, $T_{\perp e}/T_{\|e} = 0.536$, and $\beta_{\|e} = 8$, $T_{\perp e}/T_{\|e} = 0.722$. The solid circles shows the initial stages whereas the empty circles show the final ones. The dotted lines denote the corresponding constant electron kinetic energy/temperature contours. The dashed labeled lines denote contours of the constant maximum growth rates (given in units of ω_{ce}). The dash-dotted line denotes the fluid fire hose threshold condition $\beta_{\|e} - \beta_{\perp e} = 2$.

4. Discussion

Results of the 2-D Darwin PIC code show that a relatively weak oblique resonant electron fire hose instability has a self-destructive nonlinear behavior similar to its proton counterpart [*Hellinger and Matsumoto*, 2000]; it has even less complicated evolution compared to the oblique proton fire hose since it has no competing instability [*Hellinger and Matsumoto*, 2001], which appear for stronger initial growth rates [*Camporeale and Burgess*, 2008]. The weak oblique fire hose destabilizes a non-propagating branch which only exists for a sufficiently strong temperature anisotropy. The instability generates waves which in turn scatter (mainly the resonant) electrons and reduce their temperature anisotropy; as the temperature anisotropy is being reduced the non-propagating modes disappear and the waves are transformed to propagating modes which are rapidly damped. This is not a standard quasi-linear behavior but can be to some extent interpreted as a quasi-linear evolution modified by a mode conversion (and, in later stages, by wave-wave interactions). The electron oblique fire hose only weakly interacts with protons which are only weakly heated; the relative change of the proton thermal energy is of the order of 10^{-4}.

For numerical reasons we used for the PIC simulations the frequency ratio $\omega_{pe}/\omega_{ce} = 4$, which is much smaller then typical values in the solar wind. However, as the fire hose instability generates transverse waves with frequencies much smaller than ω_{ce}, we expect that this instability will have the same evolution for larger values of ω_{pe}/ω_{ce}. We used (again for numerical reasons) initial conditions with the maximum growth rate $\gamma_{max} = 5 \cdot 10^{-2}\omega_{ce}$, which are relatively weak but probably too strong for the solar wind as the electron temperature anisotropy is only slowly driven [cf. *Landi et al.*, 2012] and the instability needs to be just fast enough to counteract the anisotropy driver [cf., *Matteini et al.*, 2006; *Hellinger and Trávníček*, 2008]. We expect that for weaker growth rates the oblique electron fire hose instability has the same self-destructive evolution with (likely smaller) jumps from unstable to stable region.

The simulation results of *Gary and Nishimura* [2003] were limited by the short duration as they terminated the simulations shortly after saturation and they only reported the presence of non-propagating modes. We expect that they would get similar results, a large reduction of the fluctuating magnetic energy after the saturation and the final state would be in the stable region, far from the marginal stability; their simulations are, however, still constricted by a small simulation box which allows only a limited number of unstable modes. The simulation results of *Camporeale and Burgess* [2008] exhibit an evolution similar to what we observe. After the saturation the fluctuating magnetic energy is strongly reduced and the wave activity shifts during the nonlinear evolution to larger wavelengths and angles. *Camporeale and Burgess* [2008] also observe propagating modes which they attribute to the propagating fire hose branch which is destabilized in their cases of strong instability. Our results suggest that some of the propagating mode activity may be due to the branch change. In contrast with our results the simulations of *Camporeale and Burgess* [2008] exhibit oscillations around the marginal stability, which may be a result of small simulation boxes, strong initial growth rates and the presence of unstable competing propagating modes.

The results presented here are relevant for solar wind electrons. However, the electron velocity distribution functions have typically a more complicated form consisting of multiple populations [*Štverák et al.*, 2009], which influence the linear stability of the system and introduce other sources of free energy for kinetic instabilities. These problems will be subject of future work.

Glossary

Here subscripts $\perp$ and $\parallel$ denote the perpendicular and parallel directions with respect to the ambient magnetic field $\boldsymbol{B}_0$, $B_0 = |\boldsymbol{B}_0|$ denotes its the magnitude. Here $\boldsymbol{E}$ denotes the electric field, $\boldsymbol{v}$ denotes a velocity, $v = |\boldsymbol{v}|$ being its magnitude, and $v_\parallel$ and $v_\perp$ denote the magnitudes of the velocity components parallel and perpendicular to $\boldsymbol{B}_0$, respectively; t denotes the time, $\delta\boldsymbol{B}$ denotes the fluctuating magnetic field $\delta\boldsymbol{B} = \boldsymbol{B} - \boldsymbol{B}_0$, δB is its magnitude. Here subscripts e and p denote electrons and protons, respectively, subscript 0 denotes initial values. Here n_e denotes the electron number density, $T_{\parallel\mathrm{e}}$ and $T_{\perp\mathrm{e}}$ denote the parallel and perpendicular electron temperatures, respectively, $T_\mathrm{e} = (2T_{\perp\mathrm{e}} + T_{\parallel\mathrm{e}})/3$ is the mean electron temperature and $v_{th\parallel\mathrm{e}} = (k_B T_{\parallel\mathrm{e}}/m_\mathrm{e})^{1/2}$ is the electron parallel thermal velocity. Here $T_{\parallel\mathrm{p}}$ and $T_{\perp\mathrm{p}}$ denote the parallel and perpendicular electron temperatures, respectively, $T_\mathrm{p} = (2T_{\perp\mathrm{p}} + T_{\parallel\mathrm{p}})/3$ is the mean electron temperature. Here $\beta_{\parallel\mathrm{e}} = 2\mu_0 n_\mathrm{e} k_B T_{\parallel\mathrm{e}}/B_0^2$ is the electron parallel beta, $\omega_{ce} = eB_0/m_\mathrm{e}$ and $\omega_{pe} = (n_\mathrm{e}e^2/m_\mathrm{e}\epsilon_0)^{1/2}$ denote the electron cyclotron and plasma frequencies, respectively, and $d_\mathrm{e} = c/\omega_{pe}$ is the electron inertial length. In these expressions m_e denotes the electron mass, k_B is the Boltzmann constant, e denotes the proton charge, ϵ_0 and μ_0 denote the vacuum electric permittivity and magnetic permeability, respectively, and c denotes the speed of light. Here, $\boldsymbol{k}$ denotes the wave vector, k its magnitude, $k_\parallel$ and $k_\perp$ its parallel and perpendicular components, respectively, θ_{kB} denotes the angle between $\boldsymbol{k}$ and the ambient magnetic field. Here ρ is the charge density and $\boldsymbol{j}$ is the electric current density.

References

Camporeale, E., and D. Burgess (2008), Electron firehose instability: kinetic linear theory and 2D particle-in-cell simulations, *J. Geophys. Res.*, *113*, A07107, doi:10.1029/2008JA013043.

Decyk, V. K. (2007), UPIC: A framework for massively parallel particle-in-cell codes, *Computer Phys. Comm.*, *177*, 95–97.

Gary, S. P. (1993), *Theory of Space Plasma Microinstabilities*, Cambridge Univ. Press, New York.

Gary, S. P., and K. Nishimura (2003), Resonant electron firehose instability: Particle-in-cell simulations, *Phys. Plasmas*, *10*, 3571–3576.

Hellinger, P., and H. Matsumoto (2000), New kinetic instability: Oblique Alfvén fire hose, *J. Geophys. Res.*, *105*, 10,519–10,526.

Hellinger, P., and H. Matsumoto (2001), Nonlinear competition between the whistler and Alfvén fire hoses, *J. Geophys. Res.*, *106*, 13,215–13,218.

Hellinger, P., and P. Trávníček (2008), Oblique proton fire hose instability in the expanding solar wind: Hybrid simulations, *J. Geophys. Res.*, *113*, A10109, doi:10.1029/2008JA013416.

Hellinger, P., and P. M. Trávníček (2011), Proton core-beam system in the expanding solar wind: Hybrid simulations, *J. Geophys. Res.*, *116*, A11101, doi:10.1029/2011JA016940.

Hewett, D. W. (1985), Elimination of electromagnetic radiation in plasma simulation – the DARWIN or magnetoinductive approximation, *Space Sci. Rev.*, *42*, 29–40.

Hollweg, J. V., and H. J. Völk (1970), New plasma instabilities in the solar wind, *J. Geophys. Res.*, *75*, 5297–5309.

Ibscher, D., M. Lazar, and R. Schlickeiser (2012), On the existence of Weibel instability in a magnetized plasma. II. Perpendicular wave propagation: The ordinary mode, *Phys. Plasmas*, *19*, 072116.

Landi, S., L. Matteini, and F. Pantellini (2012), On the competition between radial expansion and Coulomb collisions in shaping the electron velocity distribution function: Kinetic simulations, *Astrophys. J.*, *760*, 143.

Lazar, M., and S. Poedts (2009), Limits for the firehose instability in space plasmas, *Solar Phys.*, *258*, 119–128.

Lazar, M., S. Poedts, R. Schlickeiser, and D. Ibscher (2013), The electron firehose and ordinary-mode instabilities in space plasmas, *Solar Phys.*, doi:10.1007/s11207-013-0348-y.

Li, X., and S. R. Habbal (2000), Electron kinetic firehose instability, *J. Geophys. Res.*, *105*, 27,377–27,386.

Matteini, L., S. Landi, P. Hellinger, and M. Velli (2006), Parallel proton fire hose instability in the expanding solar wind: Hybrid simulations, *J. Geophys. Res.*, *111*, A10101, doi:10.1029/2006JA011667.

Messmer, P. (2002), Temperature isotropization in solar flare plasmas due to the electron firehose instability, *Astron. Astrophys.*, *382*, 301–311.

Paesold, G., and A. O. Benz (1999), Electron firehose instability and acceleration of electrons in solar flares, *Astron. Astrophys.*, *351*, 741–746.

Paesold, G., and A. O. Benz (2003), Test particle simulation of the electron firehose instability, *Astron. Astrophys.*, *401*, 711–720.

Phillips, J. L., and J. T. Gosling (1990), Radial evolution of solar wind thermal electron distributions due to expansion and collisions, *J. Geophys. Res.*, *95*, 4217–4228.

Phillips, J. L., J. T. Gosling, D. J. McComas, S. J. Bame, S. P. Gary, and E. J. Smith (1989), Anisotropic thermal electron distributions in the solar wind, *J. Geophys. Res.*, *94*, 6563–6579.

Salem, C., D. Hubert, C. Lacombe, S. D. Bale, A. Mangeney, D. E. Larson, and R. P. Lin (2003), Electron properties and Coulomb collisions in the solar wind at 1 AU: Wind observations, *Astrophys. J.*, *585*, 1147–1157.

Schriver, D., et al. (2010), Generation of whistler mode emissions in the inner magnetosphere: An event study, *J. Geophys. Res.*, *115*, A00F17, doi:10.1029/2009JA014932.

Štverák, Š., P. Trávníček, M. Maksimovic, E. Marsch, A. Fazakerley, and E. E. Scime (2008), Electron temperature anisotropy constraints in the solar wind, *J. Geophys. Res.*, *113*, A03103, doi:10.1029/2007JA012733.

Štverák, Š., M. Maksimovic, P. M. Trávníček, E. Marsch, A. N. Fazakerley, and E. E. Scime (2009), Radial evolution of nonthermal electron populations in the low-latitude solar wind: Helios, Cluster, and Ulysses observations, *J. Geophys. Res.*, *114*, A05104, doi:10.1029/2008JA013883.

P. Hellinger, Astronomical Institute, AS CR, Bocni II/1401, Prague 14100, Czech Republic. (petr.hellinger@asu.cas.cz)

P. M. Trávníček, Space Sciences Laboratory, University of California, Berkeley, CA 94720, USA. (pavel@ssl.berkeley.edu)

V. K. Decyk, Department of Physics and Astronomy, University of California, Los Angeles, CA 90095, USA. (decyk@physics.ucla.edu)

D. Schriver, Department of Physics and Astronomy, Institute of Geophysics and Planetary Physics, University of California, Los Angeles, CA 90095, USA. (dave@igpp.ucla.edu)